Great Impostors: Extremely Compact, Merging Binary Neutron Stars in the Mass Gap Posing as Binary Black Holes

Antonios Tsokaros,[1,*] Milton Ruiz,[1] Stuart L. Shapiro,[1,2] Lunan Sun,[1] and Kōji Uryū[3]
[1]Department of Physics, University of Illinois at Urbana-Champaign, Urbana, Illinois 61801, USA
[2]Department of Astronomy & NCSA, University of Illinois at Urbana-Champaign, Urbana, Illinois 61801, USA
[3]Department of Physics, University of the Ryukyus, Senbaru, Nishihara, Okinawa 903-0213, Japan

(Received 15 November 2019; revised manuscript received 20 December 2019; accepted 27 January 2020; published 21 February 2020)

Can one distinguish a binary black hole undergoing a merger from a binary neutron star if the individual compact companions have masses that fall inside the so-called mass gap of 3–5 $M_\odot$? For neutron stars, achieving such masses typically requires extreme compactness and in this work we present initial data and evolutions of binary neutron stars initially in quasiequilibrium circular orbits having a compactness $C = 0.336$. These are the most compact, nonvacuum, quasiequilibrium binary objects that have been constructed and evolved to date, including boson stars. The compactness achieved is only slightly smaller than the maximum possible imposed by causality, $C_{\max} = 0.355$, which requires the sound speed to be less than the speed of light. By comparing the emitted gravitational waveforms from the late inspiral to merger and postmerger phases between such a binary neutron star vs a binary black hole of the same total mass we identify concrete measurements that serve to distinguish them. With that level of compactness, the binary neutron stars exhibit no tidal disruption up until merger, whereupon a prompt collapse is initiated even before a common core forms. Within the accuracy of our simulations the black hole remnants from both binaries exhibit ringdown radiation that is not distinguishable from a perturbed Kerr spacetime. However, their inspiral leads to phase differences of the order of ∼5 rad over an ∼81 km separation (1.7 orbits) while typical neutron stars exhibit phase differences of ≥20 rad. Although a difference of ∼5 rad can be measured by current gravitational wave laser interferometers (e.g., aLIGO/Virgo), uncertainties in the individual masses and spins will likely prevent distinguishing such compact, massive neutron stars from black holes.

DOI: 10.1103/PhysRevLett.124.071101

Introduction.—Determining the neutron star (NS) maximum mass is a one of the most fascinating, unresolved issues in modern astrophysics. The answer is intimately related to identifying the correct equation of state (EOS) that describes matter at supranuclear densities [1]. Currently the highest observed NS mass is $2.14^{+0.20}_{-0.18}\ M_\odot$ [2]. In principle, the upper limit allowing only for causality and a matching density to a well-understood EOS somewhere around nuclear density, can be as high as 4.8 $M_\odot$ [3], while recent studies based on the detection of the gravitational wave (GW) signal GW170817 place it around ∼2.2–2.3 $M_\odot$ [4–7]. All these studies adopt a number of underlying assumptions whose validity will require new observations to be verified or modified accordingly. Observationally, merging binary black holes (BHBHs), black hole-neutron stars (BHNSs), or binary neutron stars (NSNSs) whose companions have masses that fall into the mass gap range (3–5 $M_\odot$) are hard to distinguish [8–11]. The identification of a compact object becomes even more challenging when one includes exotic configurations, such as quark stars, boson stars, etc., or alternative theories of gravity.

The parameter that encodes how much mass a compact star can hold in a certain volume is the compactness, defined as the dimensionless ratio $C = GM/Rc^2$. Here M is the Arnowitt-Desser-Misner (ADM) mass, and R the areal (Schwarzschild) radius of an isolated, nonrotating star with the same baryon mass. Our sun has $C = 2 \times 10^{-6}$, a small number indicative of its nonrelativistic nature, while the upper limit, $C = 1/2$, is set by a Schwarzschild BH. Typical NSs have compactions around ∼0.1–0.2 with the precise number determined by the as yet unknown EOS. An extreme case is the incompressible fluid limit that yields $C = 4/9 = 0.4\bar{4}$, the so-called Buchdahl limit [12]. This limit is unrealistic since it predicts an infinite sound speed. If one satisfies the causality criterion for the sound speed (i.e., $c_s \leq c$) then the upper limit for compactness drops to $C_{\max} = 0.355$ [13–15].

Compact binary systems provide some of the best laboratories to test the predictions of general relativity, as well as to probe possible deviations from its description of strong gravity. Despite the large progress that has been achieved in numerical relativity we are still lacking theoretical simulations that involve extremely compact

NSs in binaries. In Ref. [16] NSNS initial data in quasiequilibrium were constructed with compactness up to $C = 0.26$ using the LORENE code [17,18]. Similarly, in Ref. [19] BHNS initial data were presented using the SpEC code [20,21] that reach the same compactness. Recently [22], NSNS initial data with compactness up to $C = 0.284$, together with preliminary evolution simulations, were computed using the SGRID code [23,24].

The purpose of this work is to quantify the difference between a BHBH and an NSNS system when the total ADM mass falls inside the mass gap and to provide useful GW diagnostics that may distinguish them. First, we construct the most massive NSNSs in quasicircular orbit with the highest compactness to date using our initial data solver COCAL [25–27]. The system has ADM mass $M = 7.90\ M_\odot$ and each star a compactness of $C = 0.336$. This value (which is even higher than the maximum possible compactness that can be achieved by solitonic boson stars [28]) is only slightly smaller than the limiting compactness $C_{\max} = 0.355$ set by causality. Second, using the ILLINOIS GRMHD code [29–32], we evolve this NSNS system and perform a detailed comparison of the gravitational waveforms with a BHBH system having the same initial ADM mass. We find that an NSNS system having the above compactness inspirals very similarly to the BHBH system and merges *without essentially any tidal disruption*. We conjecture that to be true irrespective of the EOS for this level of compaction. The merged NSNS remnant collapses to a BH even before a common core forms. Since there is no disk formation, and a negligible escaping mass, one may not expect a sGRB or a kilonova from such an NSNS event. The GW phase difference at the peak GW amplitude of the NSNS system is ~5 rad with respect to the BHBH binary inside the band [0.6,1] KHz. This phase difference corresponds to ~20% of the accumulated phase during the last ~1.7 orbits (corresponding to an initial separation of ~81 km) and *can* be detected by the aLIGO/Virgo network. On the other hand, the postmerger remnants have ringdown waveforms that *cannot* be distinguished from the Kerr BH ringdown within the accuracy of our simulations.

In the following we employ geometric units in which $G = c = M_\odot = 1$, unless stated otherwise.

EOS and numerical methods.—In this work we employ the cold EOS adopted in Ref. [33] which we called ALF2cc. It is based on the ALF2 EOS [34] where the region with rest-mass density $\rho_0 \geq \rho_{0s}$ is replaced by the maximum stiffness EOS given by

$$P = \sigma(\rho - \rho_s) + P_s. \tag{1}$$

Here σ is a dimensionless parameter, ρ is the total energy density, and P_s the pressure at ρ_s. The solutions presented in this work assume $\sigma = 1.0$, i.e., a core at the causal limit, which represents the maximally compact, compressible EOS [35]. The matching density ρ_s is, in principle, the point beyond which current nuclear studies cannot confidently describe matter and it is a multiple of nuclear matter density $\rho_{0\text{nuc}} = 2.7 \times 10^{14}$ gr/cm^3. In our current study though, we simply take $\rho_{0s} = \rho_{0\text{nuc}}$ in order to maximize the NS compactness and thereby provide a benchmark upon which future studies can be compared (see also Refs. [36,37] for other EOSs that support such high compactions).

Our NSNS initial data are computed using the COCAL code [25–27,38] while the BHBH initial data using the TWOPUNCTURES code [39,40]. For the NSNS binary each NS has a rest mass $M_0 = 5.18$, which corresponds to a spherical star with compactness $M/R = 0.336$. The ADM mass of the system is $M = 7.90$, the coordinate separation is 80.6 km, and the orbital angular velocity is $\Omega M = 0.0460$. All NS radii are approximately 10 km. Although the distance between the two NSs is very large compared with typical NSNS simulations it only results in $N \sim 1.7$ orbits prior to merger according to the lowest order post-Newtonian (PN) formula [41], $2\pi N = (M\Omega)^{-5/3}/(32\nu)$ [$\nu = m_1 m_2/(m_1 + m_2)^2 = 1/4$], due to the very large gravitational mass of the system. The challenge both for the initial data calculation, as well as for the evolution, is to resolve a relatively small and very compact NS over such a large binary separation. In Fig. 1 we plot the rest-mass density profile across the x axis that passes through the center of each star. The profiles look very similar to self-bound quark stars whose density at the surface is finite. The red horizontal line divides the region with the causal EOS Eq. (1) (above the red line) from the polytropic ALF2 crust (below the red line). The region near the surface is expanded in the inset of Fig. 1 which shows that our stars exhibit ~500 m of crust, which is ~5% of their radius but only ≤1% of the rest mass. The blue vertical line pinpoints the surface of the NS while the red lines mark the change of the EOS.

We perform evolutions of the BHBH and NSNS systems using the ILLINOIS GRMHD adaptive-mesh-refinement

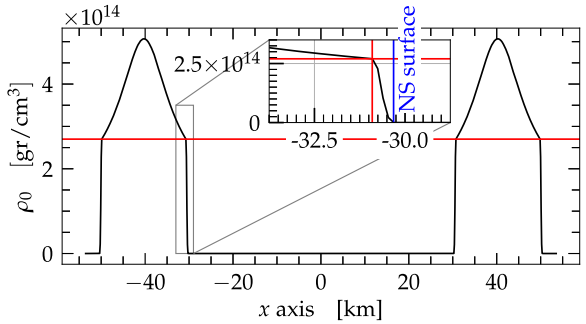

FIG. 1. Rest-mass density profile across the x axis for the NSNS system with the ALF2cc EOS. Horizontal red line corresponds to nuclear density $\rho_{0\text{nuc}}$. The inset enlarges the area close to the surface where the density drops from $\rho_{0\text{nuc}}$ to zero in a steep manner.

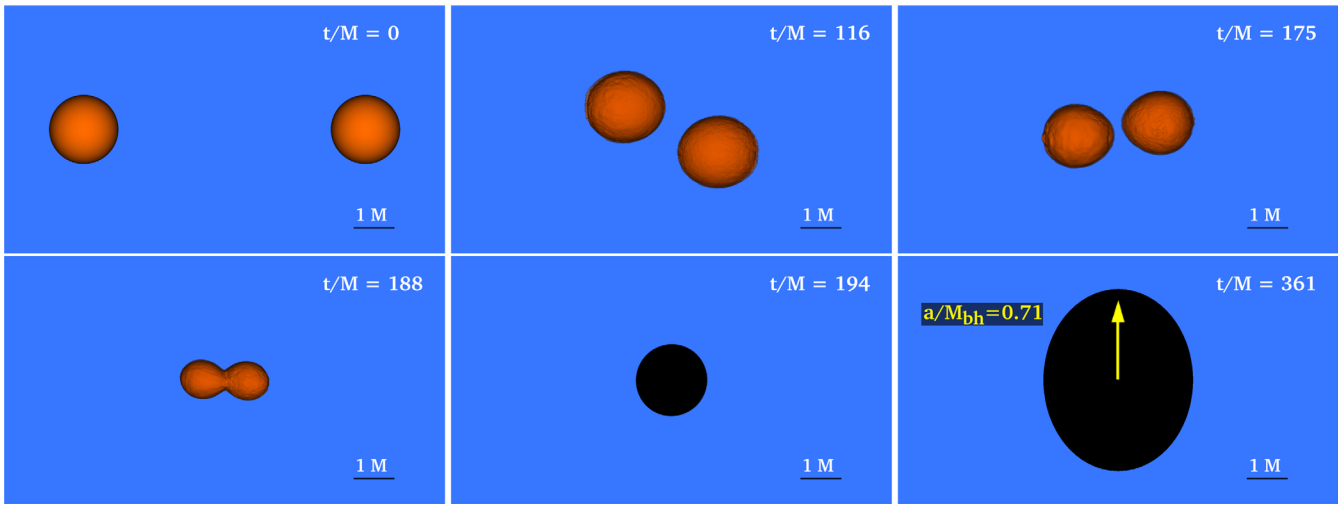

FIG. 2. Evolution of an $M = 7.90\ M_\odot$ binary NSNS system. Isocontours of rest-mass density $\rho_0 = 2.263 \times 10^{13}$ gr/cm^3, which corresponds to $0.998 R_x(0)$ and therefore is a accurate representation of the surface of the star.

code [29–32] which employs the Baumgarte-Shapiro-Shibata-Nakamura (BSSN) formulation of Einstein's equations [42–44] to evolve the spacetime metric and the matter fields (see Ref. [33] for an evolution that also adopts the ALF2cc EOS). For the NSNS binary we use two resolutions: Resolution R1nsns uses eight refinement boxes with $\Delta x_{\rm min} = 118$ m, while resolution R2nsns employs $\Delta x_{\rm min} = 98.5$ m. Both R1nsns and R2nsns can resolve the crust by four or five points (initially). In the Supplemental Material [45] we plot the violations of the constraint equations, where their peak values indeed come from the crust. Future simulations will improve the accuracy. For the BHBH binary, resolution Rbhbh uses nine refinement boxes with $\Delta x_{\rm min} = 175$ m. Reflection symmetry is imposed across the orbital plane. Both resolutions that we use are among the highest in NSNS simulations. According to Ref. [46] one needs $\Delta x_{\rm min} \leq 100$ m to achieve sub-radian accuracy ($\sim$0.2 rad) and nearly convergent waveforms in approximately 15 orbits. In our case the high compactness of our NSs necessitate the use of such resolution, while lower resolutions seem inadequate to keep the stars in bound orbits.

For the GW diagnostics we use the methods described in Ref. [47] and denote by $h^{\ell m}(t) = h_+^{\ell m}(t) - i h_\times^{\ell m}(t) = A_{\ell m}(t) e^{-i\Phi_{\ell m}(t)}$ the strain of the (ℓ, m) mode and $\omega_{\ell m} = 2\pi f_{\ell m} = d\Phi_{\ell m}/dt$ the corresponding GW frequency.

Results.—The evolution of the NSNS system is depicted in Fig. 2 where isocontours at density $\rho_0 = 2.26 \times 10^{13}$ gr/cm^3 $= \rho_0^{\rm max}(0)/22.4$ are plotted at various times during the inspiral. This isocontour corresponds to the density at a radial distance $0.998 R_x(0)$ measured from the maximum density point in the NSs; therefore it is an accurate representation of the surface of the star. In accordance with the (PN) prediction the binary performs approximately $\sim$1.7 orbits with the two stars starting as two spherical configurations to high accuracy. Tidal distortion becomes evident only at 1.5 orbits when $t/M \approx 170$. Shortly afterwards (less than a quarter of an orbit) merger begins *with no cusp formation* (cf. Ref. [48]). The surface remains intact up until the merging of the two NSs at $t/M = 180$ where they actually touch. Immediately thereafter the remnant collapses, at $t/M \sim 183$, when the structure still has a clear dumbbell shape as in the snapshot at the left column, bottom panel of Fig. 2 (with $t/M = 188$). The apparent horizon immediately after collapse has a spherical shape but settles as a prolate configuration at the end of the simulation. This is simply a gauge effect caused by the NSNS moving puncture coordinates. The ratio of polar to equatorial proper circumferences asymptotes to $\sim 0.89 < 1$ (see postmerger section) [49].

Inspiral.—In the top panel of Fig. 3 we plot the normalized strain of the (2,2) mode (r_A is the areal radius). Despite the small number of orbits performed by our NSNS system one can appreciate the fact that the early part of the inspiral is very similar for both NSNS and BHBH, with differences starting to appear when the tidal interactions begin at $t/M \sim 130$. This observation is expected since our NSs are very compact and thus have small radii R_x; at initial separations of $\sim 8 R_x$ the inspiral should develop according to the point-particle approximation. For the same reason one expects that tidal effects will start to develop later on, which is what we find. For all simulations we extract Ψ_4 at seven different radii from the orbital center and verify the expected "peeling" property $r\Psi_4 = {\rm const.}$. In the figures shown here we used an extraction radius $R_{\rm ex} = 106M = 1241$ km.

As expected, the NSNS binary merges earlier than the BHBH binary even though tidal effects are minimal. Also, by comparing the two NSNS resolutions, we observe that the NSNS evolved with the high resolution (R2nsns)

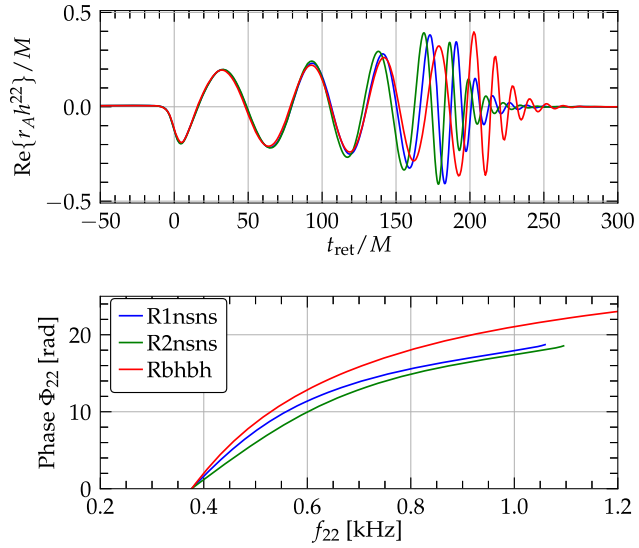

FIG. 3. Top panel: strain vs retarded time for the ($\ell = 2$, $m = 2$) dominant mode. R1nsns and R2nsns correspond to the two resolutions of the NSNS system and Rbhbh to the BHBH simulation. Bottom panel shows the phase $\Phi_{22}(t)$ of the strain up until its maximum vs the GW frequency.

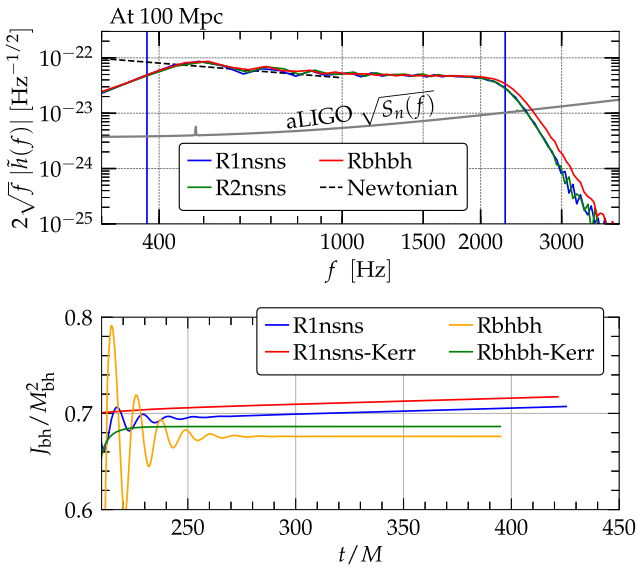

FIG. 4. Top panel: Fourier spectra of numerical waveforms (colored lines). Vertical blue lines correspond to the frequency of the (2,2) mode at the initial separation and at the ringdown. Bottom panel: Spin of the remnant BHs.

merges slightly earlier than R1nsns. In the bottom panel of Fig. 3 we plot the phase of the GW strain Φ_{22} of the (2,2) mode as a function of frequency up until the moment of maximum strain. At a given time the angular velocity of the BHBH binary is smaller than the corresponding of the NSNS binary, leading to delayed merger. Although our two NSNS resolutions produce a small phase difference between them, the important quantity here is the phase difference $\Delta\Phi_{22} = |\Phi_{22}^{\mathrm{BHBH}} - \Phi_{22}^{\mathrm{NSNS}}|$. The largest dephasing between the BHBH and NSNS curves is $\lesssim$3.5 rad within [0.6, 1.0] KHz. If we extrapolate our results to infinite resolution (see Refs. [47,50–52] and the Supplemental Material [45]) we conclude that a BHBH binary will have maximum $\sim$5 rad difference with respect to an NSNS of compaction $C = 0.336$ in the aforementioned bandwidth. This result is in accordance with other studies [47,53] where typical NSNS binaries are employed and phase differences $\gtrapprox$20 rad were recorded depending on the EOS, and the NSNS binary properties. Our maximally compact stars yield a minimal but *measurable* phase difference. Given the fact that this phase difference is produced in the last $\sim$1.7 orbits, or through an accumulated phase of only $\sim$20 rad, we calculate that the dephasing relative to the BHBH case is significant $\sim$20%.

In Fig. 4 top panel we plot the Fourier spectrum at 100 Mpc of the (2,2) mode $\tilde{h}(f) = \mathcal{F}(h^{22})$ for the NSNS (two resolutions, blue and green lines) and BHBH (red line) binaries. We also plot the aLIGO noise curve (gray line) [54], as well as the Newtonian prediction [55] (dashed lines). Vertical blue lines correspond to the initial and ringdown GW frequency of the (2,2) mode (see next section). The power spectral density for the two kind of binaries is very similar, thus in order to quantify their difference we compute the match function [56] $\mathcal{M} = \max_{(\phi_c,t_c)}[(\tilde{h}_1|\tilde{h}_2(\phi_c,t_c))/\sqrt{(\tilde{h}_1|\tilde{h}_1)(\tilde{h}_2|\tilde{h}_2)}]$ where the maximization is taken over a large set of phase shifts ϕ_c and time shifts t_c. Here $(\tilde{h}_1|\tilde{h}_2)$ denotes the standard noise-weighted inner product [56]. For both resolutions R1nsns and R2nsns we find $\mathcal{M} = 0.998$, i.e., the waveforms emitted at 100 Mpc are distinguishable with current detectors for a signal-to-noise ratio of, e.g., 25 [57,58], comparable to GW150914 [59]. However, uncertainties in the individual masses and spins will likely prevent these detectors from distinguishing these compact, massive NS binaries from BH binaries.

Postmerger.—In order to diagnose the spin of the remnant BHs we use two methods. First, using the isolated horizon formalism [60] we calculate $a/M_{\mathrm{bh}} = J_{\mathrm{bh}}/M_{\mathrm{bh}}^2$ (using R1nsns and Rbhbh for the NSNS and BHBH runs, respectively). Second, for the Kerr spacetime the ratio of proper polar horizon circumference, L_p, to the equatorial one, L_e is $L_p/L_e = 4\sqrt{r_+^2 + a^2}E[a^2/(r_+^2 + a^2)]$, where $E(x)$ is the complete elliptic integral of the second kind. Following Ref. [61] we can approximate this expression by $L_p/L_e \approx [\sqrt{1-(a/M_{\mathrm{bh}})^2} + 1.55]/2.55$. By computing the ratio L_p/L_e directly from the metric one can get an estimate of a/M_{bh} using the latter approximate formula. This quantity is plotted in the bottom panel of Fig. 4. The two spin diagnostics agree to a level of $\sim$1.5% for both binaries, while the spin of the BHBH binary remnant differs from the one of the NSNS binary remnant by $\sim$4% with the NSNS remnant BH having higher spin. This is consistent

with the calculated GW angular momentum emission and the conservation of angular momentum diagnostic shown in the Supplemental Material [45].

Although the mode frequencies $\omega_{\ell m}$ of the GW signal during inspiral and merger are described by complicated functions of time, during ringdown the GW signal can be described with high accuracy as a simple superposition of damped sinusoids characterized by three indices: the two spherical harmonic indices ℓ, m, and a third overtone index, $n = 0, 1, \ldots$, which here we assume to be the fundamental one $n = 0$ [62,63]. As a consequence of the no-hair theorem, all dimensionless mode frequencies, $M_{\rm bh}\omega_{\ell mn}$, and damping times $\tau_{\ell mn}/M_{\rm bh}$ depend only on the dimensionless spin of the remnant BH. For our BHBH and NSNS binaries the dominant modes are the (2,2) and (4,4) ones. The frequencies of the (2,2) modes for the NSNS and BHBH binaries are very close to each other and lead to a BH spin which is consistent with the values presented in Fig. 4 and discussed in the previous paragraph. In particular, we find that $(M_{\rm bh}\omega_{22})_{\rm NSNS} = 0.54$ while $(M_{\rm bh}\omega_{22})_{\rm BHBH} = 0.53$. The (4,4) modes are more noisy and yield $(M_{\rm bh}\omega_{44})_{\rm NSNS} = 1.13$ and $(M_{\rm bh}\omega_{44})_{\rm BHBH} = 1.11$.

In order to compare the ringdown of our models to well-known results from perturbation theory for Kerr BHs we use the fits provided in Ref. [63]:

$$M_{\rm bh}\omega_{22} = 1.5251 - 1.1568(1 - a/M_{\rm bh})^{0.1292},$$
$$M_{\rm bh}\omega_{44} = 2.3000 - 1.5056(1 - a/M_{\rm bh})^{0.2244}. \quad (2)$$

Using the (2,2) frequencies of our models we find $(a/M_{\rm bh})_{\rm NSNS} = 0.71$ and $(a/M_{\rm bh})_{\rm BHBH} = 0.69$ in very good agreement with the values shown in Fig. 4. The (4,4) mode predicts spins which differ by ∼5% from the ones coming from the (2,2) one. This is within the accuracy of our angular momentum conservation (see Supplemental Material [45]) but is also expected due to the larger noise in our simulation for those higher order modes. In conclusion, the ringdown of both the NSNS and BHBH binaries is consistent with the ringdown of a perturbed Kerr BH, with the mass and angular momentum of the remnants closely matching the ones predicted by the Kerr metric.

It is a pleasure to thank J. Creighton and N. Yunes for useful discussions. We thank the Illinois Relativity Group REU team, G. Liu, K. Nelli, and M. N. T Nguyen for assistance in creating Fig. 2. This work was supported by NSF Grant No. PHY-1662211 and NASA Grant No. 80NSSC17K0070 to the University of Illinois at Urbana-Champaign, as well as by JSPS Grant-in-Aid for Scientific Research (C) 15K05085 and 18K03624 to the University of Ryukyus. This work made use of the Extreme Science and Engineering Discovery Environment (XSEDE), which is supported by National Science Foundation Grant No. TG-MCA99S008. This research is part of the Blue Waters sustained-petascale computing project, which is supported by the National Science Foundation (Grants No. OCI-0725070 and No. ACI-1238993) and the State of Illinois. Blue Waters is a joint effort of the University of Illinois at Urbana-Champaign and its National Center for Supercomputing Applications. Resources supporting this work were also provided by the NASA High-End Computing (HEC) Program through the NASA Advanced Supercomputing (NAS) Division at Ames Research Center.

*tsokaros@illinois.edu

[1] J. M. Lattimer, Annu. Rev. Nucl. Part. Sci. **62**, 485 (2012).
[2] H. T. Cromartie *et al.*, Nat. Astron. **4**, 72 (2019).
[3] J. B. Hartle, Phys. Rep. **46**, 201 (1978).
[4] M. Ruiz, S. L. Shapiro, and A. Tsokaros, Phys. Rev. D **97**, 021501(R) (2018).
[5] M. Shibata, E. Zhou, K. Kiuchi, and S. Fujibayashi, Phys. Rev. D **100**, 023015 (2019).
[6] L. Rezzolla, E. R. Most, and L. R. Weih, Astrophys. J. **852**, L25 (2018).
[7] B. Margalit and B. D. Metzger, Astrophys. J. **850**, L19 (2017).
[8] M. Hannam, D. A. Brown, S. Fairhurst, C. L. Fryer, and I. W. Harry, Astrophys. J. **766**, L14 (2013).
[9] T. B. Littenberg, B. Farr, S. Coughlin, V. Kalogera, and D. E. Holz, Astrophys. J. **807**, L24 (2015).
[10] I. Mandel, C.-J. Haster, M. Dominik, and K. Belczynski, Mon. Not. R. Astron. Soc. **450**, L85 (2015).
[11] H. Yang, W. E. East, and L. Lehner, Astrophys. J. **856**, 110 (2018).
[12] H. A. Buchdahl, Phys. Rev. **116**, 1027 (1959).
[13] P. Haensel and J. L. Zdunik, Nature (London) **340**, 617 (1989).
[14] S. Koranda, N. Stergioulas, and J. Friedman, Astrophys. J. **488**, 799 (1997).
[15] J. M. Lattimer and M. Prakash, in *From Nuclei to Stars: Festschrift in Honor of Gerald E Brown*, edited by S. Lee (World Scientific Publishing Company, 2011), 1st ed., pp. 275–304.
[16] K. Taniguchi and M. Shibata, Astrophys. J. Suppl. Ser. **188**, 187 (2010).
[17] K. Taniguchi and E. Gourgoulhon, Phys. Rev. D **66**, 104019 (2002).
[18] E. Gourgoulhon, P. Grandclément, K. Taniguchi, J.-A. Marck, and S. Bonazzola, Phys. Rev. D **63**, 064029 (2001).
[19] K. Henriksson, F. Foucart, L. E. Kidder, and S. A. Teukolsky, Classical Quantum Gravity **33**, 105009 (2016).
[20] F. Foucart, L. E. Kidder, H. P. Pfeiffer, and S. A. Teukolsky, Phys. Rev. D **77**, 124051 (2008).
[21] H. P. Pfeiffer, L. E. Kidder, M. A. Scheel, and S. A. Teukolsky, Comput. Phys. Commun. **152**, 253 (2003).
[22] W. Tichy, A. Rashti, T. Dietrich, R. Dudi, and B. Brügmann, arXiv:1910.09690.
[23] W. Tichy, Classical Quantum Gravity **26**, 175018 (2009).
[24] W. Tichy, Phys. Rev. D **84**, 024041 (2011).
[25] A. Tsokaros, K. Uryū, and L. Rezzolla, Phys. Rev. D **91**, 104030 (2015).
[26] A. Tsokaros, K. Uryū, M. Ruiz, and S. L. Shapiro, Phys. Rev. D **98**, 124019 (2018).

[27] K. Uryū and A. Tsokaros, Phys. Rev. D **85**, 064014 (2012).
[28] C. Palenzuela, P. Pani, M. Bezares, V. Cardoso, L. Lehner, and S. Liebling, Phys. Rev. D **96**, 104058 (2017).
[29] Z. B. Etienne, V. Paschalidis, and S. L. Shapiro, Phys. Rev. D **86**, 084026 (2012).
[30] Z. B. Etienne, Y. T. Liu, V. Paschalidis, and S. L. Shapiro, Phys. Rev. Lett. **85**, 064029 (2012).
[31] Z. B. Etienne, V. Paschalidis, and S. L. Shapiro, Phys. Rev. D **86**, 084026 (2012).
[32] V. Paschalidis, M. Ruiz, and S. L. Shapiro, Astrophys. J. Lett. **806**, L14 (2015).
[33] A. Tsokaros, M. Ruiz, L. Sun, S. L. Shapiro, and K. Uryū, Phys. Rev. Lett. **123**, 231103 (2019).
[34] M. Alford, M. Braby, M. Paris, and S. Reddy, Astrophys. J. **629**, 969 (2005).
[35] J. M. Lattimer and M. Prakash, Phys. Rep. **621**, 127 (2016).
[36] X. Y. Lai and R. X. Xu, Mon. Not. R. Astron. Soc. **398**, L31 (2009).
[37] E. Zhou, A. Tsokaros, L. Rezzolla, R. Xu, and K. Uryū, Phys. Rev. D **97**, 023013 (2018).
[38] A. Tsokaros, B. C. Mundim, F. Galeazzi, L. Rezzolla, and K. Uryū, Phys. Rev. D **94**, 044049 (2016).
[39] M. Ansorg, B. Brügmann, and W. Tichy, Phys. Rev. D **70**, 064011 (2004).
[40] V. Paschalidis, Z. B. Etienne, R. Gold, and S. L. Shapiro, arXiv:1304.0457.
[41] L. Blanchet, Living Rev. Relativity **17**, 2 (2014).
[42] M. Shibata and T. Nakamura, Phys. Rev. D **52**, 5428 (1995).
[43] T. W. Baumgarte and S. L. Shapiro, Phys. Rev. D **59**, 024007 (1998).
[44] T. W. Baumgarte and S. L. Shapiro, *Numerical Relativity: Solving Einstein's Equations on the Computer* (Cambridge University Press, Cambridge, England, 2010).
[45] See Supplemental Material at http://link.aps.org/supplemental/10.1103/PhysRevLett.124.071101 for equation of state and evolution diagnostics.
[46] K. Kiuchi, K. Kawaguchi, K. Kyutoku, Y. Sekiguchi, M. Shibata, and K. Taniguchi, Phys. Rev. D **96**, 084060 (2017).
[47] A. Tsokaros, M. Ruiz, V. Paschalidis, S. L. Shapiro, and K. Uryū, Phys. Rev. D **100**, 024061 (2019).
[48] L. Baiotti, B. Giacomazzo, and L. Rezzolla, Phys. Rev. D **78**, 084033 (2008).
[49] Movies highlighting results of our simulations can be found at http://research.physics.illinois.edu/cta/movies/Peqrho_EOS/.
[50] Z. B. Etienne, J. A. Faber, Y. T. Liu, S. L. Shapiro, K. Taniguchi, and T. W. Baumgarte, Phys. Rev. D **77**, 084002 (2008).
[51] Z. B. Etienne, Y. T. Liu, and S. L. Shapiro, Phys. Rev. D **82**, 084031 (2010).
[52] P. L. Espino, V. Paschalidis, T. W. Baumgarte, and S. L. Shapiro, Phys. Rev. D **100**, 043014 (2019).
[53] T. Dietrich, A. Samajdar, S. Khan, N. K. Johnson-McDaniel, R. Dudi, and W. Tichy, Phys. Rev. D **100**, 044003 (2019).
[54] D. Shoemaker, LIGO Report No. LIGO-T0900288-v2, 2009, the high-power detuned model used in this paper is given in the data file ZERO_DET_HIGH_P.TXT.
[55] C. Cutler and E. E. Flanagan, Phys. Rev. D **49**, 2658 (1994).
[56] B. Allen, W. G. Anderson, P. R. Brady, D. A. Brown, and J. D. E. Creighton, Phys. Rev. D **85**, 122006 (2012).
[57] I. Harry and T. Hinderer, Classical Quantum Gravity **35**, 145010 (2018).
[58] K. Chatziioannou, A. Klein, N. Yunes, and N. Cornish, Phys. Rev. D **95**, 104004 (2017).
[59] B. P. Abbott *et al.* (LIGO Scientific and Virgo Collaborations), Phys. Rev. Lett. **116**, 061102 (2016).
[60] O. Dreyer, B. Krishnan, D. Shoemaker, and E. Schnetter, Phys. Rev. D **67**, 024018 (2003).
[61] S. R. Brandt and E. Seidel, Phys. Rev. D **52**, 870 (1995).
[62] K. D. Kokkotas and B. G. Schmidt, Living Rev. Relativity **2**, 2 (1999).
[63] E. Berti, V. Cardoso, and C. M. Will, Phys. Rev. D **73**, 064030 (2006).